J. Fluid Mech. (2013), *vol.* 717, *pp.* 449–471.
doi:10.1017/jfm.2012.586

Scaling behaviour in Rayleigh–Bénard convection with and without rotation

E. M. King[1,2,†], S. Stellmach[3] and B. Buffett[1]

[1]Department of Earth and Planetary Science, University of California, Berkeley, CA 94720-4767, USA

[2]Department of Physics, University of California, Berkeley, CA 94720-7300, USA

[3]Institut für Geophysik, WWU Münster, Corrensstrasse 24, 48149 Münster, Germany

(Received 31 May 2012; revised 7 September 2012; accepted 23 November 2012;
first published online 1 February 2013)

Rotating Rayleigh–Bénard convection provides a simplified dynamical analogue for many planetary and stellar fluid systems. Here, we use numerical simulations of rotating Rayleigh–Bénard convection to investigate the scaling behaviour of five quantities over a range of Rayleigh ($10^3 \lesssim Ra \lesssim 10^9$), Prandtl ($1 \leqslant Pr \leqslant 100$) and Ekman ($10^{-6} \leqslant E \leqslant \infty$) numbers. The five quantities of interest are the viscous and thermal boundary layer thicknesses, δ_v and δ_T, mean temperature gradients, β, characteristic horizontal length scales, ℓ, and flow speeds, Pe. Three parameter regimes in which different scalings apply are quantified: non-rotating, weakly rotating and rotationally constrained. In the rotationally constrained regime, all five quantities are affected by rotation. In the weakly rotating regime, δ_T, β and Pe, roughly conform to their non-rotating behaviour, but δ_v and ℓ are still strongly affected by the Coriolis force. A summary of scaling results is given in table 2.

Key words: Bénard convection, convection, geophysical and geological flows

1. Introduction

Convection is ubiquitous in nature, as fluids in many astro- and geophysical bodies flow to redistribute destabilizing thermal and gravitational energy stores. Rotation is also a common feature of these systems, which can strongly influence the nature of convection through the Coriolis acceleration.

We examine a simplified analogue of these systems by way of Rayleigh–Bénard convection (RBC) with and without rotation. RBC consists of a fluid layer sandwiched between two rigid, horizontal boundaries (Bénard 1900; Rayleigh 1916). The bottom boundary is warmer than the top, and the gravity vector points downwards. This temperature drop, ΔT, destabilizes the fluid layer, as cool, heavier fluid lies atop warmer, more buoyant fluid. The convection is Boussinesq; fluid properties are isotropic and fixed in time and space, except in the buoyancy force, which is driven by thermal expansion. For rotating RBC, the fluid layer is rotated about a vertical axis with constant angular frequency Ω.

† Email address for correspondence: ericmking@gmail.com

	Parameter	Definition	Simulations
Input	Rayleigh number	$Ra \equiv \alpha g \Delta T L^3/(\nu\kappa)$	$10^3 \lesssim Ra \lesssim 10^9$
	Ekman number	$E \equiv \nu/(2\Omega L^2)$	$10^{-6} \leqslant E \leqslant \infty$
	Prandtl number	$Pr \equiv \nu/\kappa$	$1 \leqslant Pr \leqslant 100$
Output	Nusselt number	$Nu \equiv qL/(k\Delta T)$	$1 \lesssim Nu \lesssim 50$
	Péclet number	$Pe \equiv UL/\kappa$	$3 < Pe < 3000$

TABLE 1. Dimensionless parameters used in the development of scaling laws. Dimensional quantities are as follows: α is the fluid's coefficient of thermal expansivity; g is gravitational acceleration; ΔT is the temperature drop across the fluid layer; L is the depth of the fluid layer; ν is the fluid's viscous diffusivity; κ is the thermal diffusivity of the fluid; Ω is the angular rotation rate; q is mean heat flux; k is the fluid's thermal conductivity; and U is a mean flow speed.

Rotating RBC is governed by the Boussinesq Navier–Stokes equations and the heat equation (e.g. Chandrasekhar 1953):

$$\frac{\partial \boldsymbol{u}}{\partial t} + \boldsymbol{u}\cdot\boldsymbol{\nabla}\boldsymbol{u} + 2\boldsymbol{\Omega}\times\boldsymbol{u} = -\frac{1}{\rho_0}\boldsymbol{\nabla}p + \alpha\boldsymbol{g}T + \nu\nabla^2\boldsymbol{u}, \tag{1.1}$$

$$\boldsymbol{\nabla}\cdot\boldsymbol{u} = 0, \tag{1.2}$$

$$\frac{\partial T}{\partial t} + \boldsymbol{u}\cdot\boldsymbol{\nabla}T = \kappa\nabla^2 T, \tag{1.3}$$

respectively, where $\boldsymbol{u}$, p and T are velocity, modified pressure and temperature fields, respectively, α and ρ_0 are the fluid's thermal expansivity and mean density such that $\partial\rho/\partial T = -\alpha\rho_0$, and ν and κ are the viscous and thermal diffusivity of the fluid.

There are five global input parameters in the governing equations: Ω, ν, κ, $g' = \alpha g \Delta T$ and L, the depth of the fluid layer, which contain two fundamental dimensions, time and length. By Buckingham's Π theorem, the system is therefore defined by three independent prognostic parameters (Barenblatt 2003), which are usually taken to be Ra, E and Pr (see table 1). The buoyancy forcing is characterized by the Rayleigh number, Ra. The period of rotation is characterized by the Ekman number, E. The Prandtl number, Pr, characterizes the fluid itself as a ratio of viscous to thermal diffusivities.

Rotating convection can be considered to occur in one of two basic regimes, rotationally constrained and weakly rotating, as evinced by global heat transfer behaviour, Nu (see table 1) (e.g. King *et al.* 2009; Schmitz & Tilgner 2010). Heat transfer by rotationally constrained convection is suppressed relative to that by convection without rotation (e.g. Rossby 1969; Liu & Ecke 2009). Heat transfer by convection in the weakly rotating regime is observed to scale similarly to that by convection without rotation (e.g. Liu & Ecke 1997; Niemela, Babuin & Sreenivasan 2010). King, Stellmach & Aurnou (2012) investigate the scaling behaviour of Nu, using measurements from laboratory experiments and numerical simulations of: (i) non-rotating convection; (ii) weakly rotating convection; and (iii) rotationally constrained convection. Transitions between the latter two regimes are observed to occur when $RaE^{3/2} \approx 10$.

Here, we extend this framework to investigate the scaling behaviour of five separate quantities calculated from numerical RBC simulations with and without rotation. The five quantities of interest are: viscous boundary layer thickness, δ_v (§ 3); thermal

boundary layer thickness, δ_T (§ 4); bulk thermal gradients, β (§ 5); typical horizontal length scale of flow, ℓ (§ 6); and typical flow speed, Pe (§ 7). The present simulations are identical to those of King *et al.* (2012), so we adopt the same distinction between dynamical regimes. Non-rotating convection is strictly defined by $E^{-1} = 0$, whereas rotating convection occurs with $E^{-1} > 0$. The rotating system is said to be weakly rotating when $Ra\,E^{3/2} > 10$ and rotationally constrained when $Ra\,E^{3/2} < 10$. The rationale behind this regime transition parametrization, as well as its alternatives, are discussed in § 8. A brief summary is given in § 9.

2. Methods

2.1. *Numerical model*

The time evolution of the velocity, pressure and temperature fields are calculated as numerical solutions of the governing equations (1.1)–(1.3) in dimensionless form:

$$\frac{E}{Pr}(\tilde{\partial}_t\tilde{\boldsymbol{u}} + \tilde{\boldsymbol{u}}\cdot\tilde{\boldsymbol{\nabla}}\tilde{\boldsymbol{u}}) + \hat{\boldsymbol{z}}\times\tilde{\boldsymbol{u}} = -\tilde{\boldsymbol{\nabla}}\tilde{p} + Ra\,E\tilde{T}\hat{\boldsymbol{z}} + E\tilde{\nabla}^2\tilde{\boldsymbol{u}}, \tag{2.1}$$

$$\tilde{\boldsymbol{\nabla}}\cdot\tilde{\boldsymbol{u}} = 0, \tag{2.2}$$

$$\tilde{\partial}_t\tilde{T} + \tilde{\boldsymbol{u}}\cdot\tilde{\boldsymbol{\nabla}}\tilde{T} = \tilde{\nabla}^2\tilde{T}, \tag{2.3}$$

where dimensionless variables and operators are designated by tildes, and $\hat{\boldsymbol{z}}$ is the vertical unit vector. The fundamental time scale is taken to be a thermal diffusion time scale, L^2/κ. The temperature field is normalized by the temperature drop imposed across the layer, ΔT.

The computational domain is a Cartesian box with periodic sidewalls (in order to approximate an infinite plane layer); rigid, no-slip top and bottom boundaries; and diameter-to-height aspect ratio, $1 \leqslant \Gamma \leqslant 4$. Temporal discretization is accomplished through a second-order, semi-implicit Adams–Bashforth backward differentiation time stepping. Fourier series are used for spatial discretization in the horizontal direction, while Chebyshev polynomials are used in the vertical direction. The ranges of input parameters accessed are given in table 1. For further details on the numerical method and validation, see Stellmach & Hansen (2008) and King *et al.* (2012).

2.2. *Measurement technique*

We define the following nomenclature for averaging: an overbar, $\overline{\cdots}$, represents time averaging; angle brackets represent spatial averaging over the entire computational domain, $\langle\cdots\rangle$, over horizontal planes, $\langle\cdots\rangle_H$, and across the vertical extent, $\langle\cdots\rangle_z$. Time averages are usually taken over hundreds of overturn times, and never less than ten; see King *et al.* (2012).

Viscous boundary layer thicknesses δ_v are calculated as the vertical distance of the first local maximum of the mean horizontal velocity profile above (below) the bottom (top) domain boundary. That is, a vertical profile for the mean magnitude of the horizontal velocity is acquired,

$$U_H(z) = \overline{\left\langle\sqrt{\tilde{u}_H^2}\right\rangle_H}, \tag{2.4}$$

where $\tilde{u}_H$ is the dimensionless horizontal velocity, and the local peaks of this profile nearest each of the top and bottom boundaries represent the edge of the top and bottom viscous boundary layers (Belmonte, Tilgner & Libchaber 1994). An example profile is shown in figure 1. The top and bottom layer thicknesses are averaged, giving the mean viscous boundary layer thickness, δ_v.

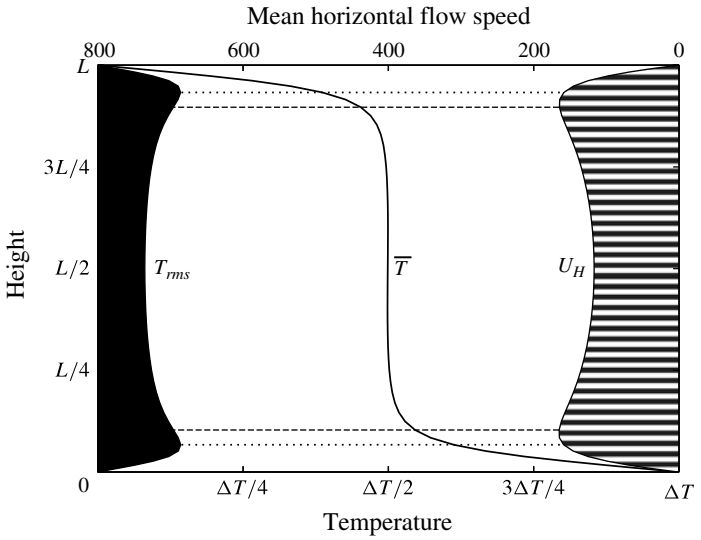

FIGURE 1. An example of profiles of mean temperature ($\overline{\langle\tilde{T}\rangle_H}$, solid line), temperature variance (T_{rms}, solid-filled curve) and mean horizontal flow speed (U_H, stripe-filled curve), from a non-rotating convection simulation with $Pr = 1$ and $Ra = 7 \times 10^5$. The horizontal dotted and dashed lines depict the calculated thickness of the thermal and viscous boundary layers, respectively.

Thermal boundary layer thicknesses δ_T are similarly calculated, using vertical profiles for mean temperature fluctuations,

$$T_{rms}(z) \equiv \overline{\left\langle \sqrt{\left(\tilde{T} - \overline{\langle\tilde{T}\rangle_H}\right)^2} \right\rangle_H}. \tag{2.5}$$

Again, local peaks in this temperature fluctuation profile give estimates for the locations of the edges of the top and bottom thermal boundary layers, whose thicknesses are averaged to calculate δ_T. An example of these profiles from a representative numerical simulation is shown in figure 1.

The typical horizontal length scale of the flow, ℓ, is defined in the following way. Let $\mathscr{E}(k, m) = [\tilde{\boldsymbol{u}}_{(k,m)}\tilde{\boldsymbol{u}}^*_{(k,m)}]$ be the dimensionless kinetic energy contained in horizontal modes k and m. The characteristic flow scales are determined by calculating the dominant horizontal wavelength of flow, ℓ, as

$$\ell^{-1} \equiv \overline{\left(\frac{\sum_{k,m} \mathscr{E}(k, m)\sqrt{k^2 + m^2}}{2\pi \sum_{k,m} \mathscr{E}(k, m)} \right)}. \tag{2.6}$$

Mean vertical temperature gradients at mid-depth are calculated as

$$\beta = \frac{\mathrm{d}}{\mathrm{d}z}\overline{\langle\tilde{T}\rangle_H}\bigg|_{z=L/2}. \tag{2.7}$$

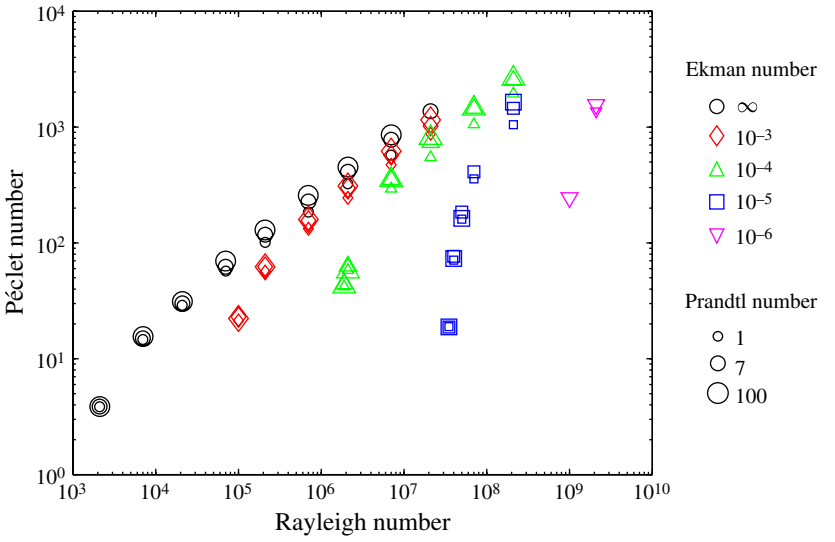

FIGURE 2. (Colour online) Péclet number versus Rayleigh number, with Ekman numbers denoted by symbol shape (and colour online), and Prandtl numbers indicated by symbol size. This figure illustrates the parameter range accessed by numerical simulations.

The Nusselt number characterizes the heat transport as

$$Nu \equiv \overline{\langle \tilde{u}_z \tilde{T} - \partial \tilde{T}/\partial \tilde{z} \rangle}, \tag{2.8}$$

and the Péclet number is defined as the typical amplitude of flow speed,

$$Pe \equiv \overline{\langle \tilde{\boldsymbol{u}} \cdot \tilde{\boldsymbol{u}} \rangle}^{1/2}. \tag{2.9}$$

Péclet number calculations are shown in figure 2 plotted versus Ra to illustrate the parameter range accessed in this study. Ekman numbers are denoted by symbol shape (and colour online), and Prandtl numbers are denoted by symbol size.

Statistical f-tests are used to distinguish quality of fit between two different scalings for identical data. An f-test assesses whether these scalings are significantly different by testing their misfits against the null hypothesis that they have equal variance to within 5 % significance. That is, the ratio of the residual variances from the two scalings is compared with 95 % confidence bounds from an f-distribution with the same degrees of freedom as these residual populations (Snedecor & Cochran 1980).

3. Viscous boundary layers, δ_v

3.1. *Non-rotating*

Viscous boundary layers in turbulent flows are commonly assumed to be of the Blasius type, derived by balancing the viscous term, which becomes important near the boundary, with the inertial term, which is thought to dominate in the bulk (e.g. Kundu 1990). Matching these terms at the edge of the boundary layer, and assuming the length scale of flow is L, gives

$$\boldsymbol{u} \cdot \nabla \boldsymbol{u} \sim \nu \nabla^2 \boldsymbol{u} \rightarrow U^2/L \sim \nu U/\delta_v^2. \tag{3.1}$$

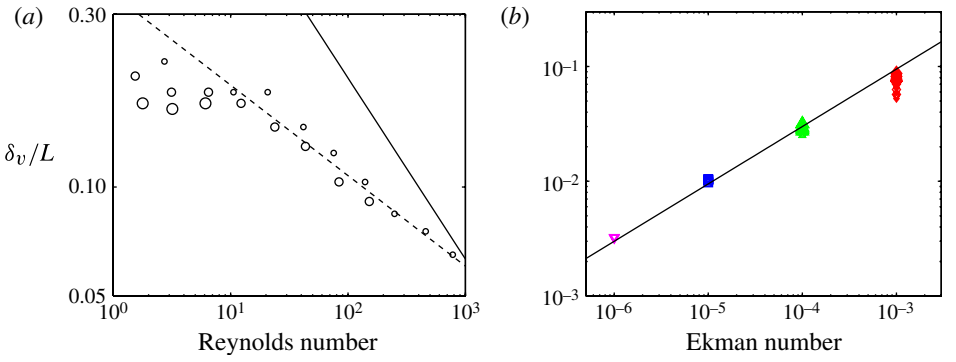

FIGURE 3. (Colour online) (*a*) Viscous boundary layer thickness versus Reynolds number, $Re = Pe/Pr$, for simulations without rotation ($E = \infty$). The solid line illustrates the slope of the predicted scaling $\delta_v \sim Re^{-1/2}L$. The dashed line shows $\delta_v = 0.34Re^{-1/4}L$. (*b*) Viscous boundary layer thickness versus the Ekman number, for rotating convection simulations. The solid black line shows $\delta_v = 3E^{1/2}L$. Symbols have the same meaning as in figure 2.

The viscous boundary layer thickness, δ_v, should then scale as

$$\delta_v \sim \sqrt{\nu L/U} = Re^{-1/2}L, \tag{3.2}$$

where $Re = Pe/Pr$ is the Reynolds number. This boundary layer scaling represents the distance over which viscosity and acceleration by Reynolds stresses act on similar time scales. A Blasius boundary layer thickness is often assumed for the development of scaling laws in non-rotating convection (e.g. Grossmann & Lohse 2000).

Figure 3(*a*) shows the thicknesses of the viscous boundary layer versus the Reynolds number from non-rotating convection simulations. The solid line shows the slope of the predicted scaling (3.2). The boundary layers within the simulations, however, are less strongly dependent on Re. A best-fit power-law regression to these data with $Re > 10$ gives

$$\delta_v = 0.34(\pm 0.05)Re^{-0.25(\pm 0.03)}L. \tag{3.3}$$

This empirical scaling law is shown as the dashed line in figure 3(*a*), and agrees with the data to within 5 % for $Re > 10$. It is not currently clear why the non-rotating viscous boundary layer scales weakly with Re, but this result is consistent with the extensive experimental study of Lam *et al.* (2002), and the numerical simulations of Breuer *et al.* (2004). We revisit this issue in the discussion section.

3.2. *Rotating*

The viscous boundary layer in rotating flows is known as an Ekman boundary layer, named after its discoverer, Ekman (1905). The scaling behaviour for the thickness of the Ekman layer comes from a balance between the Coriolis and viscous terms near the top and bottom domain boundaries:

$$2\boldsymbol{\Omega} \times \boldsymbol{u} \sim \nu\nabla^2\boldsymbol{u} \rightarrow 2U\Omega \sim \nu U/\delta_v^2. \tag{3.4}$$

The viscous boundary layer thickness, δ_v, should then scale as

$$\delta_v \sim \delta_E = \sqrt{\nu/2\Omega} = E^{1/2}L \tag{3.5}$$

in rotating convection. This boundary layer scaling represents the distance over which viscosity acts during a rotational time scale.

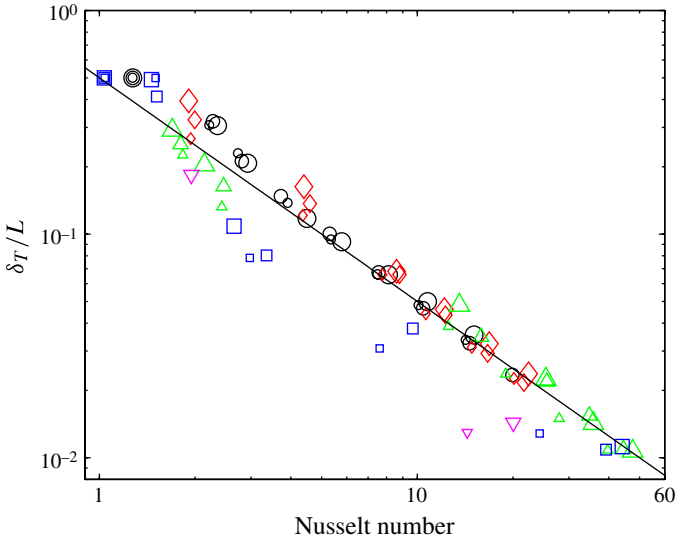

FIGURE 4. (Colour online) Thermal boundary layer thickness versus Nusselt number for convection with and without rotation. The solid line shows the slope of the predicted scaling (4.1), $\delta_T = L/(2Nu)$. Symbols have the same meaning as in figure 2.

Figure 3(*b*) shows calculations of the thickness of the viscous boundary layer plotted versus E for rotating convection. Our most rapidly rotating data appear to conform to (3.5). The solid line shows $\delta_v/L = 3E^{1/2}$, which fits the data to within 25 % on average for all rotating cases ($E \leqslant 10^{-3}$), and to within 8 % on average for $E \leqslant 10^{-4}$. Interestingly, the scaling (3.5) holds *for all* rotating convection simulations, even those with $Ra\,E^{3/2} > 10$, whose global statistics such as mean heat transport and flow speeds are no longer rotationally constrained (King *et al.* (2012), figure 6; and present work, figure 11*b*, respectively).

4. Thermal boundary layers, δ_T

4.1. *Non-rotating*

Turbulent convection, in the absence of constraining influences such as rotation, tends to mix the bulk fluid. Temperature within the interior becomes uniform as Ra is increased. The imposed temperature drop across the fluid layer is therefore accomplished almost entirely within the thermal boundary layers. The Nusselt number, Nu, is defined as the ratio of total heat transport to that by conduction alone. Conductive heat transport across the layer is given by $q_{cond} = k\Delta T/L$. The total amount of heat transported by the fluid can, in this idealized case, be related to the thickness of the boundary layer. Within the thermal boundary layer, heat transport is nearly entirely conductive, and so $q_{total} \approx k\Delta T/2\delta_T$. Thus, for turbulent, non-rotating convection, we expect (e.g. Spiegel 1971)

$$\delta_T \approx \tfrac{1}{2} Nu^{-1} L. \tag{4.1}$$

Figure 4 shows the thermal boundary layer thicknesses plotted versus Nu (non-rotating convection data are shown as circles). The solid line shows the predicted scaling (4.1),

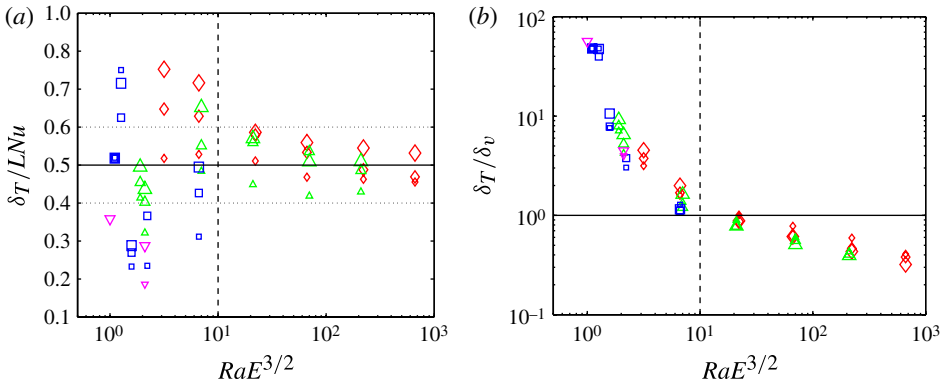

FIGURE 5. (Colour online) (*a*) Thermal boundary layer thickness normalized by the predicted scaling Nu^{-1} plotted versus the transition parameter, $Ra\,E^{3/2}$. The solid horizontal line indicates the predicted scaling (4.1), and the dotted horizontal lines indicate the standard deviation of non-rotating convection data about (4.1) (*b*) The ratio of thermal boundary layer thickness to viscous boundary layer thickness plotted versus $Ra\,E^{3/2}$ for rotating convection. The dashed vertical lines in both panels indicate the approximate location of the boundary layer crossing. Symbols have the same meaning as in figure 2.

which fits the non-rotating data to within 15 % for all cases, and to within 6 % for $Nu > 4$.

4.2. *Rotating*

In figure 4, we observe that the thermal boundary layer thickness in rotating convection is less well described by (4.1) than for convection without rotation. The quality of fit of the thermal boundary layer thickness calculations to the Nu^{-1} scaling is especially poor within the rotationally constrained regime. To see this, in figure 5(*a*) we plot $(\delta_T/L)Nu$ versus the parameter $Ra\,E^{3/2}$, which was previously defined to identify the transition between rotationally constrained and weakly rotating regimes. The solid horizontal line shows the predicted scaling for a well-mixed convective interior (4.1), and the dotted horizontal lines indicate the standard deviation of non-rotating convection data about this prediction. In the rotationally constrained regime ($Ra\,E^{3/2} < 10$), the misfit between thermal boundary layer thickness data and the classical prediction (4.1) (solid horizontal line) is 52 % on average, and can be as high as 170 %. For weakly rotating convection ($Ra\,E^{3/2} > 10$), however, the thermal boundary layer thickness data are better fitted by (4.1) with an average error of 13 % and a peak misfit of 31 %.

The poor agreement between (4.1) and rotationally constrained convection data is probably due to the breakdown of the assumption that the interior fluid is well mixed when a strong rotational influence is present. This effect of the Coriolis force has been previously observed in both experiments (e.g. Boubnov & Golitsyn 1990) and simulations (e.g. Julien *et al.* 1996, 2012). King *et al.* (2010) show that thermal mixing in geodynamo simulations can be subdued by rotation for increasingly higher Nu as E is decreased. They argue that, as the Ekman layer becomes thinner than the thermal boundary layer, the interior fluid maintains significant thermal gradients, invalidating the classical thermal boundary layer thickness scaling (4.1).

In figure 5(*b*), we plot the relative thicknesses of the thermal and Ekman boundary layers, δ_T/δ_v, calculated for all rotating convection simulations versus our predicted

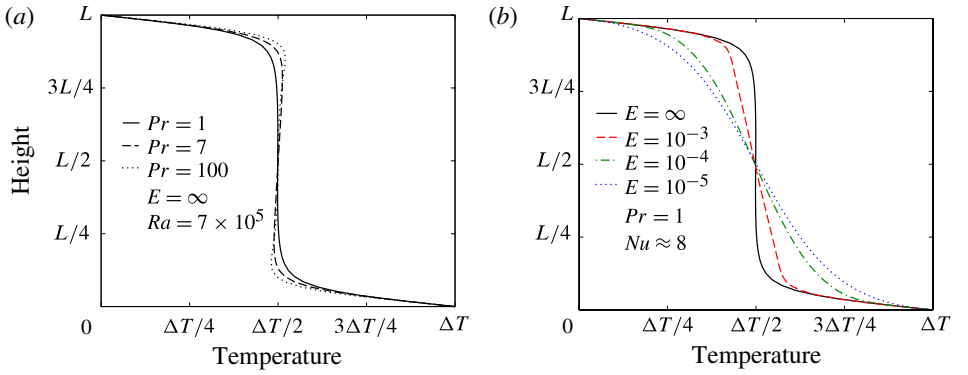

FIGURE 6. (Colour online) Mean temperature profiles for (*a*) non-rotating and (*b*) rotating convection. (*a*) Temperature profiles for non-rotating convection with $Ra = 7 \times 10^5$ and $Pr = 1$, 7 and 100. Thermal overshoot is observed as the Prandtl number is increased. (*b*) Temperature profiles for $Pr = 1$ and: $E = \infty$ (non-rotating) and $Ra = 7 \times 10^5$, solid curve, as in (*a*); $E = 10^{-3}$ and $Ra = 7 \times 10^5$, dashed curve; $E = 10^{-4}$ and $Ra = 4 \times 10^6$, dash-dotted curve; and $E = 10^{-5}$ and $Ra = 7 \times 10^7$, dotted curve. All four cases have $7.5 < Nu < 8$.

transition $Ra\,E^{3/2}$. The boundary layers swap relative positions where δ_T/δ_v crosses unity, which occurs somewhere in the range $7 < Ra\,E^{3/2} < 21$ for all Ekman and Prandtl numbers considered. We approximate this transition as $Ra\,E^{3/2} \approx 10$, shown as the dashed vertical line in figure 5. The relationship between the boundary layer thicknesses and our assumed transition parameter $Ra\,E^{3/2}$ is discussed further in § 8.2.

5. Interior temperature gradients, β

The scaling relationship between heat flux and the thermal boundary layer thickness (4.1) hinges upon the assumption that the interior fluid is well mixed. Figure 6 shows mean temperature profiles for convection simulations with and without rotation. We observe that prevailing temperature gradients vary with Pr for a given Ra in non-rotating convection (figure 6*a*), and with E for a given Pr and Nu (figure 6*b*). In order to analyse these profiles more systematically, we look at the scaling behaviour of the mean, mid-level temperature gradients, β (see (2.7)).

5.1. *Non-rotating*

Figure 7(*a*) shows β plotted versus Ra for the non-rotating simulations. Two notable observations arise. First, convection with high Rayleigh numbers ($Ra > 10^6$) and/or low Prandtl numbers ($Pr = 1$) are generally well mixed thermally (β is small). Second, the prevailing temperature gradients are *positive*, whereas the imposed global gradient is negative. This overshoot of the background gradient can be seen explicitly in the thermal profiles plotted in figure 6(*a*). Thermal overshoot has been observed previously for convection with low Re, and is attributed to convective flows dominated by long-lived thermal plumes (e.g. Olson & Corcos 1980). These plumes traverse the layer as a quasi-Stokes flow, and collect along the opposite boundary, where their temperature anomalies produce local peaks in the mean temperature profile.

5.2. *Rotating*

We observed in § 4.2 that rotation upsets the assumptions necessary to reach (4.1) (see figure 5). Previous studies have shown that the Coriolis force is capable of inhibiting

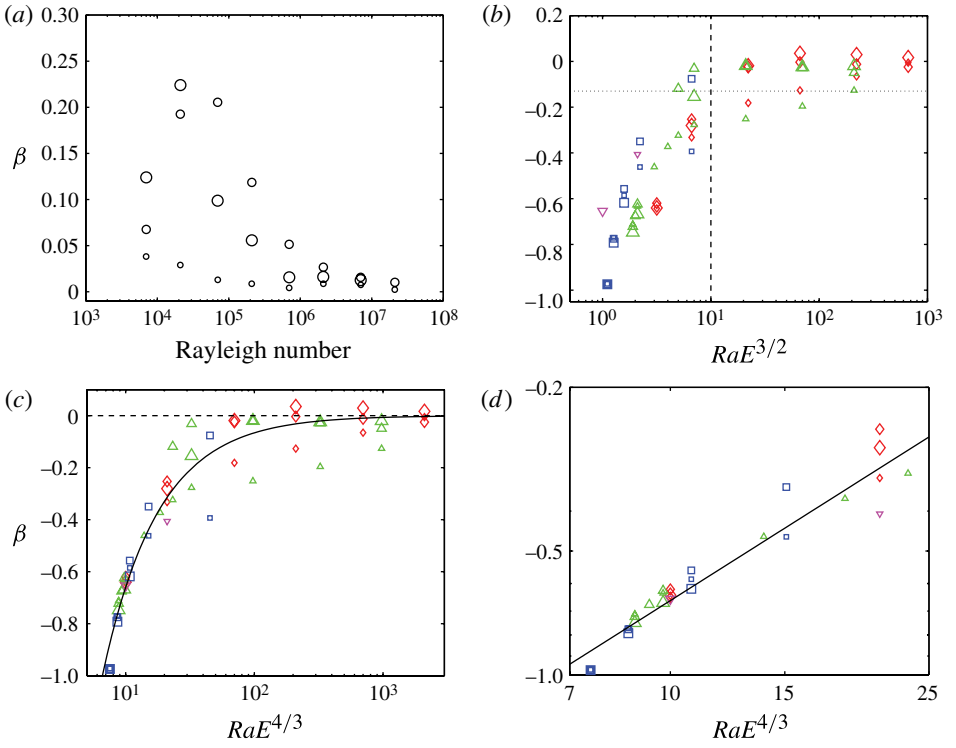

FIGURE 7. (Colour online) Interior temperature gradients (2.7) for (*a*) non-rotating and (*b–d*) rotating convection. (*a*) Temperature gradients β plotted against Ra for non-rotating convection. (*b*) Temperature gradients calculated from rotating convection simulations plotted versus the transition parameter $Ra\,E^{3/2}$. The dotted horizontal line show the mean magnitude from the non-rotating simulations in panel (*a*), $|\beta| = 0.13$. (*c*) Interior temperature gradients calculated from rotating convection simulations plotted versus $Ra\,E^{4/3}$. The solid line shows $\beta = -6.6\,(Ra\,E^{4/3})^{-1}$. (*d*) An expanded view of the same data as in panel (*c*). Symbols have the same meaning as in figure 2.

turbulent mixing in general (Taylor 1921), in convection experiments (Boubnov & Golitsyn 1990; Fernando, Chen & Boyer 1991) and simulations (Julien *et al.* 1996; Sprague *et al.* 2006; Julien *et al.* 2012), and in convective dynamo simulations (King *et al.* 2010). Understanding the interplay between rotation and thermal mixing is essential for adequate parametrization of small-scale convection in the oceans and core of the Earth and other planets.

Figure 7(*b*) shows β plotted versus $Ra\,E^{3/2}$. The dashed vertical line indicates the regime transition at $Ra\,E^{3/2} \approx 10$. The dotted horizontal line shows the mean magnitude of the mid-plane gradient for the non-rotating simulations for comparison. We observe that, in the rotationally constrained regime ($Ra\,E^{3/2} \lesssim 10$), thermal mixing is suppressed.

Figure 7(*c*,*d*) show the interior temperature gradient calculations plotted versus a measure of convective supercriticality, $Ra\,E^{4/3}$ (the onset of convection for the present range of E and Pr should occur near $Ra\,E^{4/3} = 7$ (Chandrasekhar 1953)). Sprague *et al.* (2006) observe that, near onset for an asymptotically reduced system, temperature gradients scale with the inverse of supercriticality. Our results

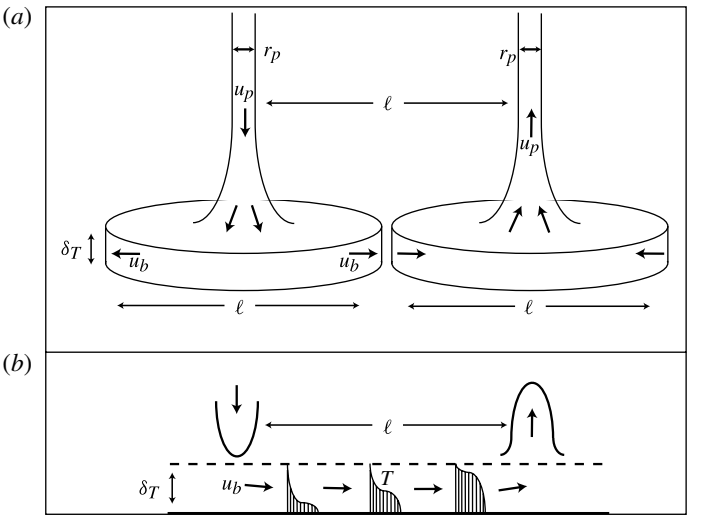

FIGURE 8. A schematic of the plume separation length scale. The typical separation between plumes is denoted by ℓ, the thermal boundary layer thickness by δ_T, typical plume speed by u_p, the typical plume width by r_p, and the flow along the boundary by u_b.

are consistent with this observation. A best-fit power-law scaling for the rotating convection simulations that have $\delta_E < 0.5\delta_T$ yields $\beta = -6.2(\pm 2.3)\,(Ra\,E^{4/3})^{-0.98(\pm 0.14)}$. On average for these rapidly rotating simulations, $\beta/(Ra\,E^{4/3}) = -6.6(\pm 1.2)$, which is shown as the solid line in figure 7(*c*,*d*), and fits these data to within 6 % on average.

6. Bulk length scales, ℓ

6.1. *Non-rotating*

It is often observed in experimental studies of Rayleigh–Bénard convection that thermal turbulence organizes into large–scale circulation patterns (also known as mean thermal winds or flywheel convection patterns) (Ahlers, Grossmann & Lohse 2009). Such aggregate patterns of thermal turbulence result from the presence of rigid sidewalls, which help to organize smaller-scale turbulence into a sweeping cell that follows the edges of the container (Xi, Lam & Xia 2004). In the present simulations, however, the absence of rigid sidewalls eliminates this selection process, and large–scale circulation patterns of this type are not observed. The length scales for flow in our simulations are instead naturally selected, and should be the typical separation of thermal plumes.

Figure 8 illustrates a simple picture of such plume separation, ℓ. We develop a scaling for ℓ by considering the distance travelled by flow along the boundary during the typical time scale for convective instability. After a cold plume impinges on the warm bottom boundary, diffusion begins to warm the fluid as it migrates across the boundary. Figure 8(*b*) schematically illustrates a series of thermal profiles within the boundary layer. The boundary flow should become unstable when the thermal anomaly grows roughly as thick as the mean thermal boundary layer, which occurs in time $\tau \sim \delta_T^2/\kappa$. In this time, the fluid travelling along the boundary at speed u_b has travelled a distance ℓ, such that

$$\ell \sim u_b \delta_T^2/\kappa. \tag{6.1}$$

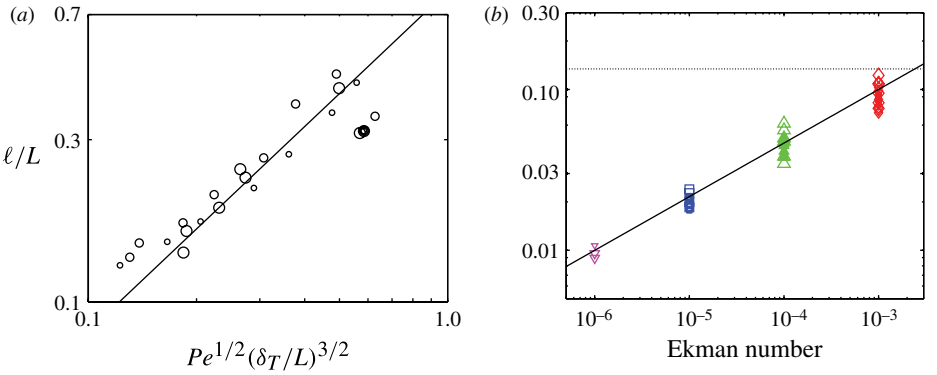

FIGURE 9. (Colour online) Characteristic length scale for (*a*) non-rotating and (*b*) rotating convection. (*a*) Plot of ℓ/L versus $Pe^{1/2}\,(\delta_T/L)^{3/2}$ (from (6.3)), from non-rotating convection simulations. The solid line shows $\ell/L = 0.8Pe^{1/2}\,(\delta_T/L)^{3/2}$. (*b*) Typical horizontal length scale versus E for rotating convection. The solid line shows $\ell = E^{1/3}L$. The horizontal dotted line shows the minimum value from the non-rotating cases, $\ell/L = 0.13$. Symbols have the same meaning as in figure 2.

Finally, we can determine how the boundary layer flow speed u_b should scale with Pe in order to estimate the characteristic length scale ℓ. Figure 8(*a*) illustrates the three-dimensional geometry of plumes and boundary layer. The plumes have radius r_p and travel vertically with speed u_p. Boundary layer flow spreads (converges) horizontally along the boundary away from impinging plumes (towards departing plumes) with speed u_b. Conservation of mass flux dictates that

$$u_p \pi r_p^2 = u_b \pi \ell \delta_T. \tag{6.2}$$

Assuming that $u_p \sim U$, and that the plume width scales with the thermal boundary layer thickness, $r_p \sim \delta_T$, we can combine (6.1) and (6.2) to estimate the natural plume spacing in non-rotating convection:

$$\ell \sim \left(\frac{\delta_T}{L}\right)^{3/2} Pe^{1/2} L. \tag{6.3}$$

A scaling law for plume spacing in high-Pr convection was developed by Parmentier & Sotin (2000) following similar reasoning. Of course, the picture presented here is simpler than expected of turbulent convection. For example, thermal plumes in RBC can be connected by thin sheets along the edge of the thermal boundary layer, which provide preferred paths for the boundary layer flow u_b, and may complicate the simple treatment presented here (e.g. Breuer *et al.* 2004; Funfschilling & Ahlers 2004).

Figure 9(*a*) shows calculations of the characteristic horizontal length scale ℓ versus this scaling (6.3) from non-rotating convection simulations. The scaling $\ell/L = 0.8Pe^{1/2}\,(\delta_T/L)^{3/2}$ is shown as a solid line, and describes the data to within 25 % on average.

An alternative, but complementary, estimate of interior length scales in non-rotating convection can be determined by heat flux considerations in the bulk. If plumes typically have radius r_p and average spacing ℓ (see figure 8), then the fraction of a horizontal cross-section through the bulk fluid occupied by plumes is $\pi\,(r_p/\ell)^2$. Mean convective heat flux, $Nu - 1 = \langle \tilde{u}'\tilde{T}' \rangle$, may scale with the typical plume speed $u_p \sim U$,

multiplied by this plume density fraction. If we again assume that the typical width of the plumes scales with the thermal boundary layer thickness, $r_p \sim \delta_T$, then

$$\ell \sim \delta_T \left(\frac{Pe}{Nu - 1} \right)^{1/2}. \tag{6.4}$$

If we further assume that the convective flow is sufficiently turbulent that $\delta_T \sim L/Nu$ and $Nu - 1 \approx Nu$, then we recover the scaling derived by considering boundary layer flow (6.3).

6.2. *Rotating*

Rotating RBC cannot be purely geostrophic, since mean convective heat transport requires vertical flow, which cannot be z-invariant in a layer of finite thickness. Convection in the presence of strong Coriolis forces must break the Taylor–Proudman (TP) theorem (Proudman 1916). For fluids with $Pr \gtrsim 1$, it is usually assumed that the TP theorem is broken by viscous forces acting on small horizontal length scales. The characteristic length scale for kinetic energy should then occur at the scale on which viscosity can balance the Coriolis term in the horizontal direction. Taking the curl of the momentum equation and retaining only these two terms, we have

$$2\Omega \frac{\partial \boldsymbol{u}}{\partial z} \sim \nu \nabla^2 \boldsymbol{\omega}, \tag{6.5}$$

where $\boldsymbol{\omega} = \nabla \times \boldsymbol{u}$ is the fluid vorticity. The next-order terms in the TP theorem tell us that $\partial/\partial z \sim 1/L$ (e.g. Greenspan 1968; King & Aurnou 2012), so the left-hand side of (6.5) scales as $\Omega U/L$. The right-hand side of (6.5), in contrast, is dominated by horizontal gradients, $\nabla^2 \omega \sim U/\ell^3$. This interior balance therefore predicts vortical flow with characteristic horizontal length scale

$$\ell/L \sim E^{1/3}. \tag{6.6}$$

This $E^{1/3}$ scale also corresponds to the critical length scale for the onset of convection in linear analysis of rapidly rotating convection (Chandrasekhar 1953), as well as the characteristic scale of convection columns in the asymptotically reduced nonlinear system of Sprague *et al.* (2006).

Figure 9(*b*) shows calculations of typical horizontal length scale ℓ/L for rotating convection plotted versus the Ekman number. A best-fit power-law scaling yields

$$\ell/L = 0.9(\pm 0.1) E^{0.33(\pm 0.02)}, \tag{6.7}$$

in agreement with the scaling prediction. The solid line in figure 9(*b*) shows $\ell/L = E^{1/3}$, which fits the rotating convection data to within an average of 2 %. Interestingly, *all* rotating cases have characteristic scales smaller than even the smallest ℓ for non-rotating convection, which is indicated by the horizontal dotted line in figure 9(*b*). This observation implies that, even in the weakly rotating regime, the scales of convective flow are dictated by the Coriolis force.

7. Flow speeds, *Pe*

7.1. *Non-rotating*

Much work has been done to relate the typical speed of convective motions (*Pe*) with the strength of driving (*Ra*) in both laboratory experiments and numerical simulations (e.g. Ahlers *et al.* 2009). A useful tool for such scaling is the exact balance between

mean global production and dissipation of kinetic energy:

$$\frac{\kappa^2}{L^4}(Nu-1)Ra = \overline{\langle(\boldsymbol{\nabla u})^2\rangle}, \tag{7.1}$$

which follows from taking the global average of $\boldsymbol{u}\cdot$(1.1) (e.g. Shraiman & Siggia 1990). The dissipation term can be approximated as either U^2/ℓ^2 or $U^2/\delta_v^2(2\delta_v/L)$, by assuming that the relevant length scale for dissipation is either the characteristic interior length scale, ℓ, or the boundary layer thickness, δ_v, respectively (Grossmann & Lohse 2000). The factor of $2\delta_v/L$ in the latter accounts for the volume fraction of the viscous boundary layers. Unfortunately, direct calculations of dissipation within the non-rotating simulations reveal no regimes in which dissipation is clearly dominated by either the bulk or the boundary layers, in agreement with Calzavarini *et al.* (2005). So we consider contributions from both bulk and boundary layers, and substitution of each of the above approximations into (7.1) produces scalings for convective speed based on dissipation in the bulk,

$$Pe^*_{int} \equiv (Nu-1)^{1/2}\,Ra^{1/2}(\ell/L), \tag{7.2}$$

and dissipation in the boundary layers,

$$Pe^*_{bl} \equiv (Nu-1)^{1/2}\,Ra^{1/2}\,(\delta_v/2L)^{1/2}\,. \tag{7.3}$$

Figure 10(*a*,*b*) show Péclet number calculations plotted versus these dissipation integral scalings. A best-fit power-law regression to each gives the expression $Pe = 0.28(\pm0.06)\,(Pe^*_{int})^{1.04(\pm0.04)}$ for the bulk dissipation estimate, and $Pe = 0.31(\pm0.05)\,(Pe^*_{bl})^{0.92(\pm0.02)}$ for the boundary layer dissipation estimate. Imposing linear fits, we get $Pe/Pe^*_{int} = 0.36(\pm0.05)$ and $Pe/Pe^*_{bl} = 0.31(\pm0.05)$, which are shown in figure 10(*a*,*b*), respectively. An f-test reveals that these fits have statistically indistinguishable differences. In other words, both scalings yield equivalent estimates for flow speeds.

These scalings suggest that convective flow may strike a balance between dissipation in the bulk and boundary layers. Such a balance can also be seen in the mean heat equation,

$$\frac{\partial}{\partial z}\overline{\langle u_z T'\rangle_H} = \kappa\frac{\partial^2}{\partial z^2}\overline{\langle T\rangle_H}, \tag{7.4}$$

where T' is a typical temperature fluctuation. Assuming an isothermal interior and well-defined thermal boundary layers, the advection and diffusion terms will each dominate within the bulk and boundary layers, respectively. Equipartition between the two is reached near the edge of the thermal boundary layer (Julien *et al.* 2012), such that we might scale (7.4) as $U\Delta T/L \approx \kappa\Delta T/\delta_T^2$. Using (4.1), this balance gives a Péclet number scaling in terms of the Nusselt number alone,

$$Pe \approx 4Nu^2. \tag{7.5}$$

Figure 10(*c*) shows Pe plotted versus Nu. A best-fit power-law regression yields $Pe = 2.0(\pm0.3)Nu^{2.11(\pm0.07)}$. When $Nu > 4$, for which (4.1) was shown to hold, our data agree better with (7.5), as $Pe = 3.1(\pm0.8)Nu^{1.93(\pm0.11)}$. Imposing a scaling of the form (7.5) gives $Pe/Nu^2 = 2.5(\pm0.4)$, which gives an average misfit of 21 % for all non-rotating data and 11 % for $Nu > 4$, and is shown as the solid line in figure 10(*c*). We caution, though, that, since this scaling is derived solely from the heat equation, it is unlikely to hold for very large Reynolds numbers, when inertia is expected to play a

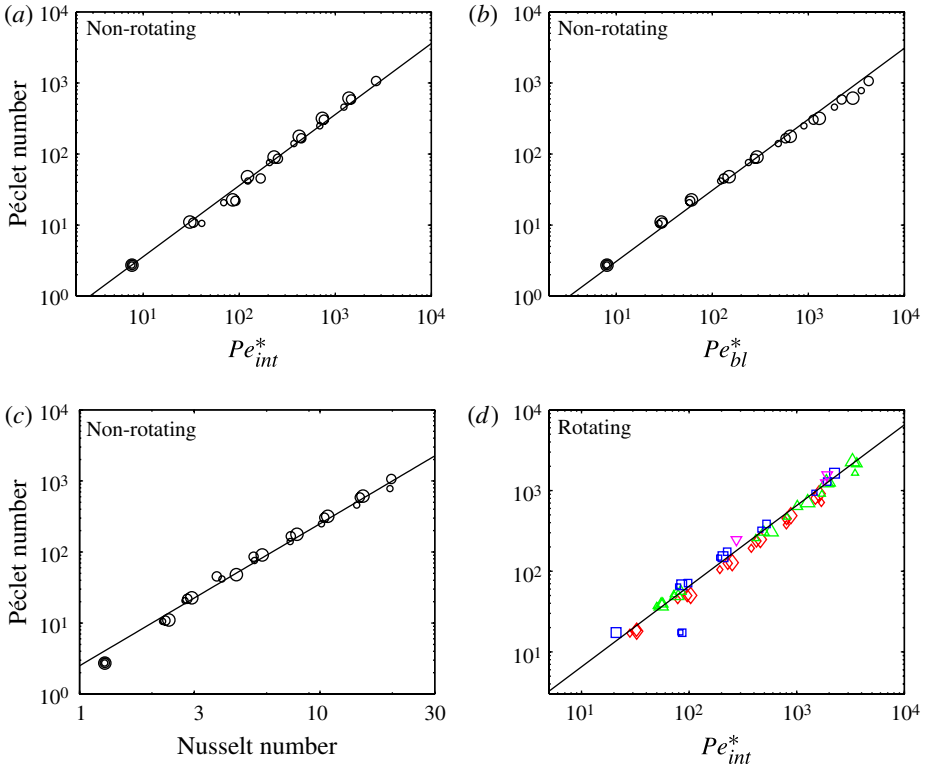

FIGURE 10. (Colour online) Péclet number scalings for (*a–c*) non-rotating and (*d*) rotating convection. (*a*) Péclet number versus the interior dissipation scaling, $Pe^*_{int} = \sqrt{Ra(Nu-1)}(\ell/L)$, for non-rotating convection. The solid line shows the scaling $Pe = 0.36Pe^*_{int}$. (*b*) Péclet number versus the boundary layer dissipation scaling, $Pe^*_{bl} = \sqrt{Ra(Nu-1)}\delta_v/2L$, for non-rotating convection. The solid line shows $Pe = 0.21Pe^*_{bl}$. (*c*) Péclet number versus the Nusselt number for non-rotating convection. The solid line shows $Pe = 2.5Nu^2$. (*d*) Péclet number versus the interior dissipation scaling, $Pe^*_{int} = \sqrt{Ra(Nu-1)}(\ell/L)$, for rotating convection. The solid line shows $Pe = 0.65Pe^*_{int}$. Symbols have the same meaning as in figure 2.

dominant role. And we do observe that the quality of the fit declines for decreasing Pr and increasing Ra.

7.2. *Rotating*

As the rate of rotation increases (decreasing E), we find that viscous dissipation is increasingly dominated by its interior (bulk) contribution, owing to the reduced characteristic length scales of bulk convection (figure 9*b*), and the ever smaller volume fraction occupied by the Ekman boundary layers (figure 3*b*). We therefore expect that flow speeds will follow the interior dissipation scaling (7.2). Figure 10(*d*) shows calculations of convective flow speed Pe plotted versus the interior dissipation scaling (7.2). A best-fit power-law regression yields $Pe = 0.62(\pm 0.14)\,(Pe^*_{int})^{0.99(\pm 0.04)}$ for all rotating convection simulations, in agreement with the prediction (7.2). The average value of Pe/Pe^*_{int} is 0.65, which is shown as the solid line in figure 10(*d*), and fits all of the rotating convection data with an average error of 36 %.

The Coriolis force can do no work, and so only enters the energetic flow speed scaling (7.2) through its influence on length scales. Fortunately, the characteristic length scales of rapidly rotating convection follow well-known scaling relationships in terms of E alone (6.6). Substituting (6.6) into (7.2) produces (e.g. Aubert *et al.* 2001; Gillet & Jones 2006) a prediction for flow speed based on the input parameter E rather than calculations of length scales:

$$Pe \sim Pe^*_{VAC} \equiv (Nu - 1)^{1/2} Ra^{1/2} E^{1/3}. \tag{7.6}$$

Here, the subscript '*VAC*' stands for *visco-Archimedean–Coriolis*, for the triple force balance on which it is based. This scaling provides a similar quality of fit to the scaling using actual, calculated length scales, and so is not plotted here. Best-fit power-law regressions yield $Pe = 0.9(\pm 0.2)\,(Pe^*_{VAC})^{0.94(\pm 0.03)}$ for all rotating convection simulations, and $Pe = 0.66(\pm 0.04)\,(Pe^*_{VAC})^{1.01(\pm 0.01)}$ for rotationally constrained simulations ($Ra\,E^{3/2} < 10$), in agreement with the prediction (7.6). The average value of Pe/Pe^*_{VAC} for $Ra\,E^{3/2} < 10$ is 0.75, and $Pe = 0.75 Pe^*_{VAC}$ fits all of the rotating convection data with an average error of 43 %, and fits the rotationally constrained cases ($Ra\,E^{3/2} < 10$) to within 8 % on average.

8. Discussion

8.1. *Composite scaling laws*

Many of the scaling laws presented here can be combined to produce new scalings without reducing agreement with data. For example, combining (7.5) with (6.3) and (4.1) generates a scaling for the characteristic length scale in non-rotating convection as a function of the thermal boundary layer thickness alone,

$$\ell/L \sim (\delta_T/L)^{1/2}. \tag{8.1}$$

This scaling describes the data as well as (6.3): with a prefactor of 0.73, it fits the non-rotating data to within 16 % on average (and quality of fit improves with increasing Ra). Furthermore, this scaling is identical to that observed by Parmentier & Sotin (2000) and Zhong (2005).

Similarly, for the non-rotating viscous boundary layer thickness, we can combine (3.3), (7.5) and the classical heat transfer scaling, $Nu \sim Ra^{1/3}$, to produce

$$\delta_v/L \sim Ra^{-1/6} Pr^{1/4}. \tag{8.2}$$

We emphasize that this scaling is empirically based, since we offer no theoretical explanation for (3.3). This relationship is, however, in close agreement with the empirical scaling observed in Lam *et al.* (2002), whose non-rotating experiments span the ranges $10^6 \lesssim Ra \lesssim 10^{11}$ and $10^{-2} \lesssim Pr \lesssim 10^3$, as well as the numerical work of Breuer *et al.* (2004), who utilize a similar geometry to ours, but reach $Re \approx 2 \times 10^4$. We feel that this agreement substantiates our finding that $\delta_v/L \sim Re^{-1/4}$ rather than the typical Blasius scaling, $\delta_v/L \sim Re^{-1/2}$. This difference is important, as many theoretical treatments of the turbulent convection problem assume the latter (e.g. Grossmann & Lohse 2000). We suggest that the Blasius scaling is not observed in these simulations and experiments because the boundary layer is active, rather than a passive response to bulk turbulence assumed in (3.1) and (3.2). Qiu & Xia measure viscous boundary layer thicknesses along both the sidewall (Qiu & Xia 1998*a*) and bottom (Qiu & Xia 1998*b*) boundaries. They find that the sidewall boundary layer has Blasius-type Re dependence, while the bottom boundary layer thickness has a weaker dependence,

scaling closer to (8.2). (For Boussinesq convection, we expect the same to hold for the top boundary.) This supports the argument that the top and bottom boundary layers, through which heat is fluxed, are dynamically active and so have thicknesses that scale differently from the Blasius type. At the sidewall, however, which is insulating, one might expect that the boundary layer is a passive response to bulk turbulence. The Blasius boundary layer scaling is also recovered in experiments where a strong mean wind is imposed by the tank geometry (Sun, Cheung & Xia 2008).

Our simulations use periodic sidewall boundary conditions in order to eliminate the effects of sidewalls, which are absent in the original formulation of the Bénard problem. The results of the non-rotating convection simulations shown here suggest that the important length scales in RBC, δ_T, δ_v and ℓ, are dynamically interdependent. Combining (3.3), (7.5) and (4.1), we get another scaling relationship for the viscous boundary layer thickness in non-rotating convection,

$$\delta_v/L \sim (\delta_T/L)^{1/2}\, Pr^{1/4}. \tag{8.3}$$

Scaling relationships (8.1) and (8.3) describe the connections between these length scales.

Rotating convection is somewhat simpler in this regard, as the scaling behaviour of δ_v and ℓ are well-behaved responses to particular balances between the Coriolis force and viscosity. The opposite is true for δ_T. In non-rotating convection the interior is effectively mixed such that (4.1) roughly holds. In rotating convection, the Coriolis force inhibits this mixing, permitting finite interior temperature gradients (figure 7), and complicating the usual depiction of heat transfer as being throttled by δ_T alone.

Of course, care must be taken when amalgamating or extrapolating the scalings presented here. For example, for non-rotating flow speeds, we can combine (7.5) and (4.1) with $Nu \sim Ra^{1/3}$ to get

$$Pe \sim Ra^{2/3}. \tag{8.4}$$

If, however, we instead use (4.1), (7.2) and (8.1), we get, in the limit of high Nu,

$$Pe \sim Ra^{1/2}. \tag{8.5}$$

We emphasize in § 7.1 that (7.5), and therefore (8.4), is likely to hold only for low Re (high Pr and/or low Ra). We expect that (8.5) should, in contrast, hold for high Re. Experiments (Lam *et al.* 2002) and simulations (Silano, Sreenivasan & Verzicco 2010) exploring broad ranges of Pr observe a transition from (8.4) to (8.5) as Pr is decreased, in support of this expectation.

In developing the simple Pe–Ra scalings (8.4) and (8.5), Nu–Ra scaling laws are used to eliminate the Nu dependence in (7.2) and (7.3). If, instead, we maintain the Nu dependence in the Pe scaling for non-rotating convection, we find better convergence. Using (4.1) with (7.2) and (8.1) (or, equivalently, with (7.3) and (8.3) and neglecting the weak Pr dependence in the latter), we arrive at

$$Pe \sim (Ra - Ra/Nu)^{1/2}\,. \tag{8.6}$$

This scaling law is shown in figure 11(*a*) with a prefactor of 0.18, which fits the non-rotating convection data to within 14 % on average.

8.2. *Regime transitions*

Previous work has investigated transitions in heat transfer behaviour for rotating convection by comparing Nu from rotating and non-rotating experiments and

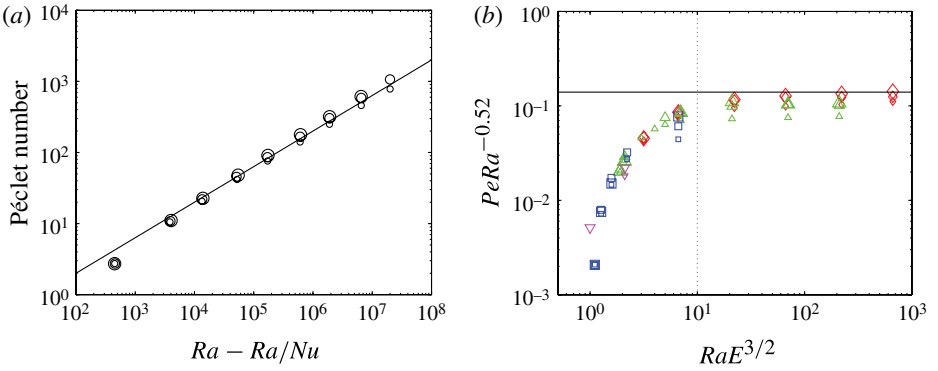

FIGURE 11. (Colour online) (*a*) Péclet number plotted versus $Ra - Ra/Nu$ from (8.6) for non-rotating convection. The solid line depicts $Pe = 0.2\,(Ra - Ra/Nu)^{1/2}$. (*b*) Transition between rotating and non-rotating flow speed behaviours. Péclet numbers from rotating convection simulations are normalized by the non-rotating fit $Ra^{0.52}$ and plotted against the boundary layer transition parameter. The solid horizontal line shows the non-rotating fit, $Pe = 0.14Ra^{0.52}$. The dotted vertical line indicates the boundary layer transition from figure 5(*b*). Symbols have the same meaning as in figure 2.

simulations (e.g. King *et al.* 2009; Liu & Ecke 2009; Zhong, Stevens & Clercx 2009). We can do the same for flow speeds, Pe. First, we must characterize the non-rotating Pe behaviour in a simple way. For this, we take a best-fit power-law regression of Pe with Ra for $E = \infty$ and $Ra > 10^5$, which yields $Pe = 0.14(\pm 0.1)Ra^{0.52(\pm 0.04)}$. Figure 11(*b*) shows flow speeds from rotating convection simulations normalized by this scaling, $Pe\,Ra^{-0.52}$, plotted versus the transition parameter, $Ra\,E^{3/2}$. We observe a change in behaviour between suppressed flow speeds and flow speeds that conform to the non-rotating behaviour (indicated by the horizontal line) near $Ra\,E^{3/2} \approx 10$, similar to the heat transfer and thermal mixing transitions observed in King *et al.* (2012) and figure 7(*b*), respectively. In contrast with the transition parameter $Ra\,E^{3/2}$, these transitions are not well described by the oft-used convective Rossby number, $Ro_c = \sqrt{Ra\,E^2/Pr}$.

Regarding heat transfer behaviour, recent work has argued that the transition between the rotationally constrained and weakly rotating regimes is related to the relative thicknesses of the thermal and Ekman boundary layers (King *et al.* 2009, 2010). Rotationally constrained convection, they argue, should occur when the Ekman boundary layer is thinner than the thermal boundary layer. When, instead, the thermal boundary layer is thinner, the influence of rotation should be weak. The two boundary layers are observed to cross when $Ra\,E^{3/2} \approx 10$; see figure 5(*b*).

Simulations of rotating convection with free-slip boundary conditions, however, produce regime transitions similar to those with no-slip boundaries (King *et al.* 2009; Schmitz & Tilgner 2010). Schmitz & Tilgner (2009) and Julien *et al.* (2012) argue that the Ekman layer cannot be responsible for these transitions, since no Ekman layer exists along free-slip boundaries. Despite this claim, Schmitz & Tilgner (2009) observe transitions that depend on a factor $E^{1/2}$, indicating a critical balance between viscous and rotational time scales similar to that of the Ekman layer. King *et al.* (2012) develop heat transfer scaling laws by assuming that the thermal boundary layer is marginally stable, i.e. assuming that a Rayleigh number defined using length scale

δ_T is equal to a similarly defined critical Rayleigh number. The convective regime, they argue, is then determined by whether buoyancy must overcome the stabilizing influence of either the Coriolis or viscous force, the former leading to rotationally constrained convection, and the latter producing a Nu scaling independent of E. Because the viscous force is scale-dependent, the relative strengths of these forces is a function of the distance from the boundary layer, and should be roughly equal at a distance $\sqrt{\nu/\Omega}$. The marginal stability of δ_T, therefore, suggests that the transition between rotationally constrained and weakly rotating convection regimes should occur when δ_T/δ_E crosses unity (δ_E is the Ekman layer thickness; see (3.5)), regardless of the mechanical boundary conditions.

Another way to formulate this regime transition is by considering the time scale for plume development. If plumes depart from the thermal boundary layer at a rate faster than the global rotation rate, one might expect that the rotational influence on that plume and, by extension, the interior convection dynamics, is secondary. In contrast, plumes taking many rotation periods to develop may be effectively 'spun-up', resulting in rotationally constrained convection. Assuming that the plume departure time scale is set by viscous flow through the thermal boundary layer, $\tau_p = \delta_T^2/\nu$ (King 2009), the transition between these two regimes occurs when $\tau_p\Omega \sim (\delta_T/\delta_E)^2$. This competition between plume and rotational time scales, however, makes no assumption about the nature of the mechanical boundary conditions. It may be, then, that the measured ratio between thermal and viscous boundary layer thicknesses in the present work is a manifestation of the important time scales for instability, rather than the control mechanism portrayed by King *et al.* (2009). We save a detailed analysis of plume behaviour for future work.

One perhaps surprising result of note is that our quantification of the influence of rotation does not agree with that by the oft-used Rossby number. Not to be confused with the convective Rossby number, the Rossby number, $Ro = (Pe\,E/Pr)(L/\ell)$, (sometimes called the local Rossby number on account of the 'locally' defined length scale ℓ) uses observed flow speeds and scales to characterize the relative importance of inertial and Coriolis forces. It is often assumed that fluid systems with low Rossby number ($Ro < 1$) are rotationally constrained. We find instead that the influence of rotation on the quantities of interest here is better described by the transition parameter $Ra\,E^{3/2}$. In our simulations, for example, we observe weakly rotating convection cases ($Ra\,E^{3/2} > 10$) that have Rossby numbers as small as $Ro \approx 10^{-3}$. We find that this difference is largely due to Prandtl number effects. Combining (7.6) with the rotationally constrained heat transfer law $Nu \sim Ra^3E^4$ of King *et al.* (2012), and assuming that $Nu - 1 \approx Nu$, gives

$$Ro \sim Ro^* = \left(Ra\,E^{3/2}\right)^2 Pr^{-1} \tag{8.7}$$

for the rotationally constrained regime. Calculations of Ro from rotationally constrained simulations ($Ra\,E^{3/2} < 10$) are well fitted by (8.7) as follows: $Ro = 0.0028(\pm 0.0004)\,(Ro^*)^{0.96(\pm 0.07)}$. Our results therefore indicate that, for $Pr \gtrsim 1$, low-Rossby-number convection is not necessarily rotationally constrained.

Much of the limitation in achieving numerical solutions of the governing equations of convection for very small E arises from the small length scales (Ekman boundary layers) and fast time scales (inertial waves) that must be resolved. Such computational difficulties have been partially overcome by the development (Julien, Knobloch & Werne 1998) and simulation (Sprague *et al.* 2006; Julien *et al.* 2012) of a reduced set of equations that implicitly incorporate the anisotropic nature of rotating convection,

permitting Ekman boundary layers and inertial waves to be 'filtered out'. As such, the reduced equations are thought to hold in the limit $E \to 0$, where Ekman boundary layers are assumed passive and inertial waves cross the container instantaneously. Solving these reduced equations numerically, Julien *et al.* (2012) find four different rotationally constrained regimes, whose boundaries depend on Ra and Pr. They predict that the rotational constraint on convection is lost when $Ra\,E^{8/5}$ is roughly unity. This transition parameter is similar to the $Ra\,E^{3/2}$ used here and in King *et al.* (2012).

Perhaps the most straightforward direct comparison between the present work and simulations of this reduced system is through scaling laws for Nu. Julien *et al.* (2012) find $Nu \sim (Ra\,E^{4/3})^{\gamma}$, with $\gamma \lesssim 2.2$, in simulations of the reduced equations, whereas King *et al.* (2012) reach a steeper, $\gamma = 3$, scaling in simulations of the full equations. On the one hand, this discrepancy could arise from the fact that the latter (present) simulations do not operate at asymptotically low E. On the other hand, some assumptions made in reducing the full equations may not be valid. For example, experiments and simulations of convection at low, but non-zero, E have consistently reported the important role of the Ekman layer in actively enhancing the transport of heat through a mechanism known as Ekman pumping (e.g. Rossby 1969; Kunnen, Clercx & Geurts 2006; Niemela *et al.* 2010). This effect could, in principle, explain the decreased slope of the Nu scaling law found in Julien *et al.* (2012) relative to King *et al.* (2012). Future work on lower-E experiments and simulations, as well as simulations of similarly reduced equations that incorporate Ekman pumping, may help to settle this question.

As a final note of interest, the scaling behaviour of rotating viscous boundary layer thicknesses, δ_v (figure 3*b*), and characteristic length scales, ℓ (figure 9*b*), are not strongly affected by the transition observed in heat transfer (King *et al.* 2012, figure 6), thermal mixing (figure 7*b*) and flow speeds (figure 11*b*). We have that Nu, β and Pe are nearly independent of rotation when $RaE^{3/2} \gtrsim 10$, whereas δ_v and ℓ are each well described by a single scaling, (3.5) and (6.6), respectively, across all of the rotating convection simulations in this study. Of course, as $RaE \to \infty$, all rotational influence must be lost, but no such transition from weakly rotating to non-rotating behaviour is observed in these simulations. We speculate that such a transition should occur near $Ro = 1$.

9. Summary

We investigate the scaling behaviour of five quantities produced in rotating and non-rotating convection simulations in a Cartesian box with periodic sidewalls, operating within the parameter ranges $10^{-6} \leqslant E \leqslant \infty$, $1 \leqslant Pr \leqslant 100$ and $10^3 \lesssim Ra \lesssim 10^9$. The quantities of interest are the viscous boundary layer thickness, δ_v, thermal boundary layer thickness, δ_T, mid-layer mean temperature gradient, β, characteristic bulk length scale, ℓ, and mean flow speeds, Pe. Our results are summarized in Table 2.

We find three important convection regimes: rotationally constrained convection, $Ra\,E^{3/2} \lesssim 10$, where heat transfer, thermal mixing and flow speeds are suppressed by the Coriolis force; weakly rotating convection, $10 \lesssim RaE^{3/2} < \infty$, where heat transfer, thermal mixing and flow speeds are not strongly affected by rotation, but δ_v and ℓ are still dictated by the Coriolis force; and non-rotating convection, $E^{-1} = 0$. The transition from rotationally constrained to weakly rotating convection occurs when the thermal boundary layer becomes thinner than about $E^{1/2}L$.

https://doi.org/10.1017/jfm.2012.586 Published online by Cambridge University Press

Regime	Geostrophic $Ra\,E^{3/2} < 10$ (35 cases)		Weakly rotating $Ra\,E^{3/2} < 10$ (39 cases)		Non-rotating $E = \infty$ (25 cases)	
Parameter	Scaling	Ref.	Scaling	Ref.	Scaling	Ref.
Nu	Ra^3E^4	King *et al.* (2009)	$Ra^{2/7}$	King *et al.* (2009)	$Ra^{2/7}$	King *et al.* (2009)
δ_v	$E^{1/2}$	Figure 3(*b*)	$E^{1/2}$	Figure 3(*b*)	$Nu^{-1/2}Pr^{1/4}$	(4.1) and (8.3)
δ_T	Nu^{-1} ?	Figures 4 and 5(*a*)	Nu^{-1}	Figure 5(*a*)	Nu^{-1}	Figure 4
β	$-(Ra\,E^{4/3})^{-1}$	Figure 7(*c*,*d*)	$\to 0$	Figure 7(*b*)	$\to 0$	Figure 7(*a*)
ℓ	$E^{1/3}$	Figure 9(*b*)	$E^{1/3}$	Figure 9(*b*)	$Nu^{-1/2}$	(4.1) and (8.1)
Pe	$((Nu-1)Ra)^{1/2}\,E^{1/3}$	(7.6)	$((Nu-1)Ra)^{1/2}\,E^{1/3}$	(7.6)	$(Ra - Ra/Nu)^{1/2}$	Figure 11(*a*)

TABLE 2. Summary of results. Regarding the weakly and non-rotating heat transfer scalings, we stress that the $2/7$ law is empirical, and probably increases with Ra to a $1/3$ law (e.g. Niemela & Sreenivasan 2006; Niemela *et al.* 2010). Also, as $Ra\,E \to \infty$, all scalings should become independent of rotation; however, a transition between weakly rotating and non-rotating behaviour is not observed here.

Acknowledgements

We thank three anonymous reviewers for helping to improve the presentation of this work. We also thank E. Knobloch, K. Julien, J. Aurnou, A. Jackson and J. Noir for fruitful discussions. E.M.K. acknowledges the support of the Miller Institute for Basic Research in Science. S.S. was supported by DFG grant HA 1765/15-2.

REFERENCES

AHLERS, G., GROSSMANN, S. & LOHSE, D. 2009 Heat transfer and large-scale dynamics in turbulent Rayleigh–Bénard convection. *Rev. Mod. Phys.* **81**, 503–537.

AUBERT, J., BRITO, D., NATAF, H. & CARDIN, P. 2001 A systematic experimental study of rapidly rotating spherical convection in water and liquid gallium. *Phys. Earth Planet. Inter.* **128**, 51–74.

BARENBLATT, G. I. 2003 *Scaling*. Cambridge University Press.

BELMONTE, A., TILGNER, A. & LIBCHABER, A. 1994 Temperature and velocity boundary layers in turbulent convection. *Phys. Rev.* E **50** (1), 269–280.

BÉNARD, H. 1900 Étude expérimentale des courants de convection dans une nappe liquide – régime permanent: tourbillons cellulaires. *J. Phys. Théor. Appl.* **9**, 513–524.

BOUBNOV, B. & GOLITSYN, G. 1990 Temperature and velocity-field regimes of convective motions in a rotating plane fluid layer. *J. Fluid Mech.* **219**, 215–239.

BREUER, M., WESSLING, S., SCHMALZL, J. & HANSEN, U. 2004 Effect of inertia in Rayleigh–Bénard convection. *Phys. Rev.* E **69** (2), 026302.

CALZAVARINI, E., LOHSE, D., TOSCHI, F. & TRIPPICCIONE, R. 2005 Rayleigh and Prandtl number scaling in the bulk of Rayleigh–Bénard turbulence. *Phys. Fluids* **17**, 055107.

CHANDRASEKHAR, S. 1953 The instability of a layer of fluid heated below and subject to Coriolis forces. *Proc. R. Soc. Lond.* A **217** (1130), 306–327.

EKMAN, V. 1905 On the influence of the Earth's rotation on ocean currents. *Ark. Mat. Astron. Fys.* **2**, 1–53.

FERNANDO, H. J. S., CHEN, R. R. & BOYER, D. L. 1991 Effects of rotation on convective turbulence. *J. Fluid Mech.* **228**, 513–547.

FUNFSCHILLING, D. & AHLERS, G. 2004 Plume motion and large-scale circulation in a cylindrical Rayleigh–Bénard cell. *Phys. Rev. Lett.* **92** (19), 194502.

GILLET, N. & JONES, C. 2006 The quasi-geostrophic model for rapidly rotating spherical convection outside the tangent cylinder. *J. Fluid Mech.* **554**, 343–369.

GREENSPAN, H. 1968 *The Theory of Rotating Fluids*. Cambridge University Press.

GROSSMANN, S. & LOHSE, D. 2000 Scaling in thermal convection: a unifying theory. *J. Fluid Mech.* **407**, 27–56.

JULIEN, K., KNOBLOCH, E. & WERNE, J. 1998 A new class of equations for rotationally constrained flows. *Theor. Comput. Fluid Dyn.* **11**, 251–261.

JULIEN, K., LEGG, S., MCWILLIAMS, J. & WERNE, J. 1996 Rapidly rotating turbulent Rayleigh–Bénard convection. *J. Fluid Mech.* **322**, 243–273.

JULIEN, K., RUBIO, A. M., GROOMS, I. & KNOBLOCH, E. 2012 Statistical and physical balances in low Rossby number Rayleigh–Bénard convection. *Geophys. Astrophys. Fluid Dyn.* **106** (4–5), 392–428.

KING, E. M. 2009 An investigation of planetary convection: the role of boundary layers. PhD thesis, University of California, Los Angeles.

KING, E. M. & AURNOU, J. M. 2012 Thermal evidence for Taylor columns in turbulent rotating Rayleigh–Bénard convection. *Phys. Rev.* E **85**, 016313.

KING, E., SODERLUND, K., CHRISTENSEN, U. R., WICHT, J. & AURNOU, J. M. 2010 Convective heat transfer in planetary dynamo models. *Geochem. Geophys. Geosyst.* **11** (6), Q06016.

KING, E. M., STELLMACH, S. & AURNOU, J. M. 2012 Heat transfer by rapidly rotating Rayleigh–Bénard convection. *J. Fluid Mech.* **691**, 568–582.

KING, E., STELLMACH, S., NOIR, J., HANSEN, U. & AURNOU, J. 2009 Boundary layer control of rotating convection systems. *Nature* **457** (7227), 301–304.

KUNDU, P. K. 1990 *Fluid Mechanics*. Academic Press.

KUNNEN, R., CLERCX, H. & GEURTS, B. 2006 Heat flux intensification by vortical flow localization in rotating convection. *Phys. Rev.* E **74** (5), 4.

LAM, S., SHANG, X.-D., ZHOU, S.-Q. & XIA, K.-Q. 2002 Prandtl number dependence of the viscous boundary layer and the Reynolds numbers in Rayleigh–Bénard convection. *Phys. Rev.* E **65** (6), 066306.

LIU, Y. M. & ECKE, R. E. 1997 Heat transport scaling in turbulent Rayleigh–Bénard convection: effects of rotation and Prandtl number. *Phys. Rev. Lett.* **79** (12), 2257–2260.

LIU, Y. & ECKE, R. 2009 Heat transport measurements in turbulent rotating Rayleigh–Bénard convection. *Phys. Rev.* E **80** (3), 6314–6325.

NIEMELA, J. J., BABUIN, S. & SREENIVASAN, K. R. 2010 Turbulent rotating convection at high Rayleigh and Taylor numbers. *J. Fluid Mech.* **649**, 509.

NIEMELA, J. J. & SREENIVASAN, K. R. 2006 Turbulent convection at high Rayleigh numbers and aspect ratio 4. *J. Fluid Mech.* **557**, 411–422.

OLSON, P. & CORCOS, G. M. 1980 A boundary layer model for mantle convection with surface plates. *Geophys. J. R. Astron. Soc.* **62**, 195–219.

PARMENTIER, E. M. & SOTIN, C. 2000 Three-dimensional numerical experiments on thermal convection in a very viscous fluid: implications for the dynamics of a thermal boundary layer at high Rayleigh number. *Phys. Fluids* **12** (3), 609–617.

PROUDMAN, J. 1916 On the motions of solids in a liquid possessing vorticity. *Proc. R. Soc. Lond.* A **96** (642), 408–424.

QIU, X. L. & XIA, K.-Q. 1998*a* Spatial structure of the viscous boundary layer in turbulent convection. *Phys. Rev.* E **58** (5), 5816.

QIU, X. L. & XIA, K.-Q. 1998*b* Viscous boundary layers at the sidewall of a convection cell. *Phys. Rev.* E **58** (1), 486–491.

RAYLEIGH, LORD 1916 On convection currents in a horizontal layer of fluid, when the higher temperature is on the under side. *Phil. Mag. Ser. 6* **32** (192), 529–546.

ROSSBY, H. 1969 A study of Bénard convection with and without rotation. *J. Fluid Mech.* **36** (2), 309–335.

SCHMITZ, S. & TILGNER, A. 2009 Heat transport in rotating convection without Ekman layers. *Phys. Rev.* E **80** (1), 5305–5307.

SCHMITZ, S. & TILGNER, A. 2010 Transitions in turbulent rotating Rayleigh–Benard convection. *Geophys. Astrophys. Fluid Dyn.* **104**, 481–489.

SHRAIMAN, B. I. & SIGGIA, E. D. 1990 Heat transport in high-Rayleigh-number convection. *Phys. Rev.* A **42** (6), 3650–3653.

SILANO, G., SREENIVASAN, K. R. & VERZICCO, R. 2010 Numerical simulations of Rayleigh–Bénard convection for Prandtl numbers between 10^1 and 10^4 and Rayleigh numbers between 10^5 and 10^9. *J. Fluid Mech.* **662**, 409–446.

SNEDECOR, G. W. & COCHRAN, W. G. 1980 *Statistical Methods*. Iowa State University Press.

SPIEGEL, E. 1971 Convection in stars. I. Basic Boussinesq convection. *Annu. Rev. Astron. Astrophys.* **9**, 323–352.

SPRAGUE, M., JULIEN, K., KNOBLOCH, E. & WERNE, J. 2006 Numerical simulation of an asymptotically reduced system for rotationally constrained convection. *J. Fluid Mech.* **551**, 141–174.

STELLMACH, S. & HANSEN, U. 2008 An efficient spectral method for the simulation of dynamos in Cartesian geometry and its implementation on massively parallel computers. *Geochem. Geophys. Geosyst.* **9** (5).

SUN, C., CHEUNG, Y. H. & XIA, K.-Q. 2008 Experimental studies of the viscous boundary layer properties in turbulent Rayleigh–Bénard convection. *J. Fluid Mech.* **605**, 79–113.

TAYLOR, G. I. 1921 Experiments with rotating fluids. *Proc. R. Soc. Lond.* A **100** (703), 114–121.

XI, H., LAM, S. & XIA, K. 2004 From laminar plumes to organized flows: the onset of large–scale circulation in turbulent thermal convection. *J. Fluid Mech.* **503**, 47–56.

ZHONG, S. 2005 Dynamics of thermal plumes in three-dimensional isoviscous thermal convection. *Geophys. J. Intl* **162** (1), 289–300.

ZHONG, J., STEVENS, R. & CLERCX, H. 2009 Prandtl-, Rayleigh-, and Rossby-number dependence of heat transport in turbulent rotating Rayleigh–Bénard convection. *Phys. Rev. Lett.* **102**, 044502.